Published on 04 July 2017. Downloaded by National Institutes of Standards & Technology on 2/26/2019 10:30:16 PM.

Lab on a Chip

PAPER

View Article Online
View Journal | View Issue

Check for updates

Cite this: *Lab Chip*, 2017, **17**, 2674

# Modeling electrical double-layer effects for microfluidic impedance spectroscopy from 100 kHz to 110 GHz†‡

Charles A. E. Little,[ab] Nathan D. Orloff,[b] Isaac E. Hanemann,[c] Christian J. Long,[b] Victor M. Bright[a] and James C. Booth *[b]

Received 30th March 2017,
Accepted 30th June 2017

DOI: 10.1039/c7lc00347a

rsc.li/loc

Broadband microfluidic-based impedance spectroscopy can be used to characterize complex fluids, with applications in medical diagnostics and in chemical and pharmacological manufacturing. Many relevant fluids are ionic; during impedance measurements ions migrate to the electrodes, forming an electrical double-layer. Effects from the electrical double-layer dominate over, and reduce sensitivity to, the intrinsic impedance of the fluid below a characteristic frequency. Here we use calibrated measurements of saline solution in microfluidic coplanar waveguide devices at frequencies between 100 kHz and 110 GHz to directly measure the double-layer admittance for solutions of varying ionic conductivity. We successfully model the double-layer admittance using a combination of a Cole–Cole response with a constant phase element contribution. Our analysis yields a double-layer relaxation time that decreases linearly with solution conductivity, and allows for double-layer effects to be separated from the intrinsic fluid response and quantified for a wide range of conducting fluids.

## 1 Introduction

Impedance spectroscopy has been used to characterize a wide variety of chemical and biological systems. Microfluidic-based impedance spectroscopy has shown specific relevance for medical diagnostics in the area of cytometry,[1–11] as well as for DNA and protein analysis.[12,13] In addition, the high throughput capability of microfluidic-based impedance spectroscopy is advantageous for pharmaceutical and chemical manufacturing. Many samples that are relevant to impedance spectroscopy have ionic components. When electric fields are applied to the fluid as part of the impedance spectroscopy measurement, free ions in solution migrate toward the electrodes. As these ions build up, an electrical double-layer (EDL) forms at the surface of the electrodes (Fig. 1). The EDL results in a large capacitance between the electrode and fluid, screening electric fields from the bulk of the fluid, thereby reducing measurement sensitivity to the intrinsic fluid impedance. The ability to distinguish device-specific EDL effects from the intrinsic fluid response is a major challenge for microfluidic impedance spectroscopy, especially at lower frequencies.

The strong frequency dependence of the EDL contribution to the total device impedance suggests that by measuring over a sufficiently wide frequency range, we can separate electrode effects from the intrinsic fluid response. At sufficiently high frequencies, EDL effects become negligible; higher frequency measurements give information primarily about the dielectric response of the fluids. However, impedance measurements above ~300 MHz can be difficult, requiring guided wave

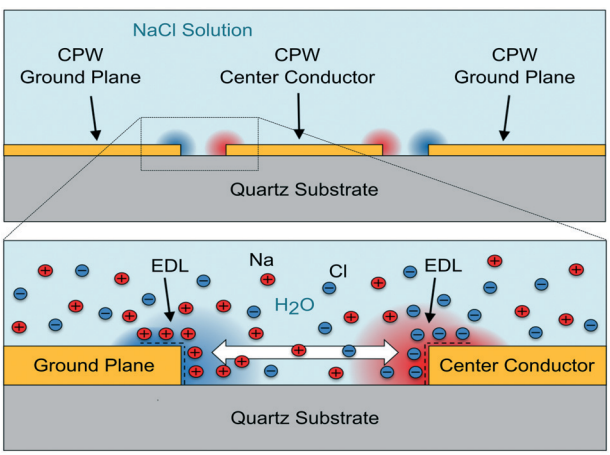


Fig. 1 Depiction of the EDL formation. During measurement, ions in the NaCl solution accumulate on the edges of the CPW electrodes.

[a] *Department of Mechanical Engineering, University of Colorado, Boulder, Colorado 80309, USA*
[b] *Communications Technology Laboratory, National Institute of Standards and Technology, Boulder, Colorado 80305, USA. E-mail: james.booth@nist.gov*
[c] *Department of Physics, University of Colorado, Boulder, Colorado 80309, USA*

† This paper is an official contribution of NIST; not subject to copyright in the US. Usage of commercial products herein is for information only; it does not imply recommendation or endorsement by NIST.

‡ Electronic supplementary information (ESI) available. See DOI: 10.1039/c7lc00347a



This journal is © The Royal Society of Chemistry 2017

Published on 04 July 2017. Downloaded by National Institutes of Standards & Technology on 2/26/2019 10:30:16 PM.

structures and detailed microwave calibrations. Previous work has demonstrated microwave impedance measurements of fluids within microfluidic channels up to a frequency of 40 GHz using coplanar waveguide (CPW) devices with on-chip microwave calibration methods.[14–17] To further extend the high frequency range of the on-chip calibration approaches, we have fabricated a new generation of microfluidic CPW devices, and developed a new efficient calibration protocol, which we present for the first time in this work. Our devices and calibration protocol allow for calibrated broadband impedance measurements of fluids over a continuous frequency range between 100 kHz and 110 GHz, capturing the full relaxation response of water, and allowing for a more complete characterization of the dielectric response of fluids.

The 6-decade frequency range provided by our devices and calibration protocol uniquely captures both the low-frequency regime where EDL effects are dominant as well as the high-frequency regime where EDL effects are negligible. We apply this technique to measure the complex electrical impedance of NaCl solutions (saline) in microfluidic devices over a range of temperatures and NaCl concentrations. We can accurately model the intrinsic fluid impedance of saline at high frequencies where EDL effects are negligible, and subsequently extrapolate this fluid response to lower frequencies where EDL effects dominate. In this way, we are able to isolate the EDL contribution to the impedance from the intrinsic fluid impedance, for solutions with different ionic conductivities. The frequency dependence of the experimentally-determined EDL impedance can then be accurately modelled by a combination of a Cole–Cole response together with a constant phase element (CPE).[18–22] These models yield a double-layer relaxation time that is inversely proportional to solution conductivity, with other model parameters showing relatively little change for different solutions. This suggests that device-dependent double-layer effects in microfluidic devices can be quantitatively accounted for based on measurements at a single value of solution conductivity.

# 2 Methods

### 2.1 Device fabrication

The on-chip calibration protocol required multiple CPW structures. We co-fabricated both microfluidic CPW structures and all additional calibration structures on the same 500 μm thick 7.62 cm diameter fused silica (quartz) wafer. Co-fabrication minimizes variability in the material properties and dimensions among CPW structures. We chose fused silica for its low electrical conductivity and isotropic permittivity. We fabricated coplanar waveguide structures on two separate chips: a test chip containing all microfluidic CPW structures, and a reference chip containing all CPW structures without microfluidics (bare CPW). Metallization was done by electron beam evaporation (Ti (5 nm)\Au (500 nm)). Bare CPW structures were designed to have a nominal characteristic impedance of ~50 Ω, with 50 μm-wide center conductors, 5 μm-wide gaps, and 200 μm-wide ground planes (Fig. 2). The series resistor and series capacitor structures, mentioned later in the calibration section, were located on the reference chip. The series resistor consisted of a 10 μm wide strip of Ti (1.5 nm)\PdAu (11 ± 0.5 nm), spanning a 10 μm gap in the center conductor of a short length of transmission line. The resulting sheet resistance of series resistor strip was measured to be ~50 Ω. The series capacitor was identical in structure to the series resistor, with the exception that the resistive materials was omitted.

We designed devices with two-layer microfluidic channels (Fig. 2). The bottom layer was made of ~50 μm of SU-8 photoresist, patterned directly over the CPW structures. The SU-8 microfluidic channels were ~80 μm wide, and 0.5, 0.85, 1.55, and 3.314 mm long. We chose the CPW gap width and SU-8 channel height so that the electromagnetic fields primarily interact with fluids contained within the SU-8 channels rather than the fluid contained within the upper microfluidic channel layer formed in polydimethylsiloxane (PDMS). We used soft lithography[23] to pattern additional microfluidic channels in a sheet of PDMS. We then cut the sheet of PDMS into individual ~1 × 0.5 cm blocks. The height of the PDMS channels was ~50 μm. After dicing the wafer into individual chips, we placed PDMS blocks on top of the SU-8 layer under a microscope. An external clamping system, consisting of an acrylic press bar screwed into an aluminum chuck, sealed the PDMS block to the chip (Fig. 2A). Liquid in the devices flows through both the upper PDMS and lower SU-8 channels in series (Fig. 2B). The upper PDMS layer routs fluid above the ground plane sections of the CPW to fill each SU-8 channel while keeping the fluid out of the range of the electromagnetic fields (Fig. 2C). Our microfluidic CPW devices had four physically distinct sections (Fig. 2E): a bare CPW section with nothing over the CPW (Fig. 2E section-1a), a bare CPW section with a PDMS roof (Fig. 2E section-1b), a CPW section completely covered with SU-8 and PDMS (Fig. 2E section-2), and the SU-8 channel section (Fig. 2E section-3). Sections 1a and 1b are electrically equivalent.

### 2.2 Measurements

We measured each CPW structure using a vector network analyzer (VNA) and movable microwave probes. We recorded raw data as complex scattering parameters (*S*-parameters) as a function of frequency. We acquired 512 frequency points from 100 kHz to 110 GHz on a log frequency scale, at an AC power of −20 dBm (where 0 dBm corresponds to a power of 1 milliwatt), and with an intermediate frequency (IF) bandwidth of 50 Hz. All measurements were performed on a temperature controlled stage. Care was taken to perform all calibrations and measurements in thermal equilibrium. The chips and aluminum block were kept on the stage for a minimum of 5 minutes after the stage reached the desired temperature set-point. After measurements were performed on the reference and empty test devices, fluid was injected into the channels and held for at least 1 minute at zero flow rate

Published on 04 July 2017. Downloaded by National Institutes of Standards & Technology on 2/26/2019 10:30:16 PM.

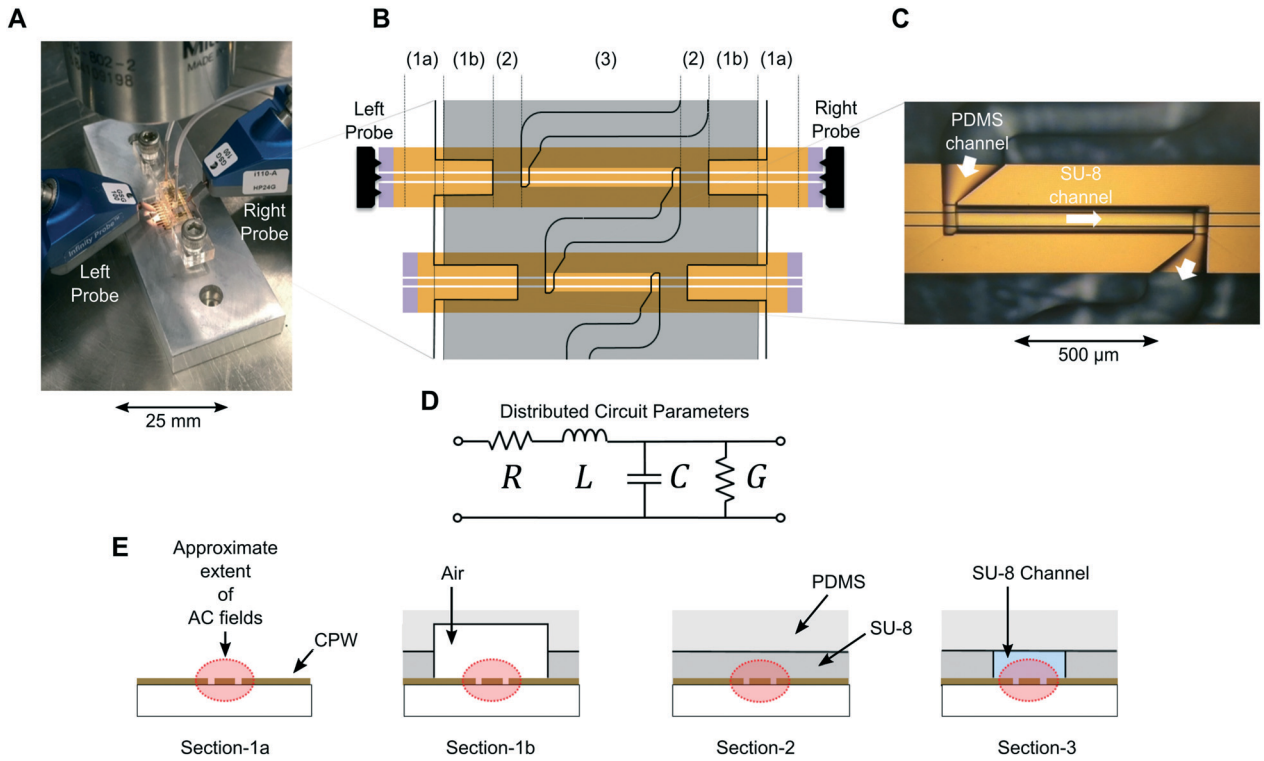


**Fig. 2** Device design and measurement setup. (A) Image of devices during measurement; left and right probes are shown. (B) Top-view diagram of device design; numbers relate to calibration sections. (C) Microscope image of microfluidic channels with arrows indicating direction of fluid flow. (D) Circuit model that describes the electrical behavior of the CPW. The distributed circuit parameters *R*, *L*, *C*, *G* are frequency dependent per unit length quantities, which are different for each calibration section. (E) Cross-section diagrams for each calibration section.

prior to fluid measurements. The temperature of the fluid was determined by measuring the temperature at the surface of the aluminum block with a thermocouple at each temperature set-point. The small thermal mass of the chip and fluid sample ensured that the sample was at thermal equilibrium with the aluminum block.

We model our measurement devices as uniform sections of transmission line cascaded together. We then apply broadband calibration and analysis procedures (described below) to transform measured *S*-parameters to distributed circuit parameters for each transmission line segment (Fig. 2D). The goal of our calibration procedures was to isolate the distributed circuit parameters for the fluid-loaded transmission-line segments (Fig. 2E section-3), over as broad a range of frequencies as possible.

### 2.3 Calibrations

We divided the calibration procedure into two steps, referred to as a two-tier calibration. For the first-tier calibration, we measured *S*-parameters for seven different bare CPW lengths (0.420, 1.000, 1.735, 3.135, 4.595, 7.615, and 9.970 mm), a series resistor, a series capacitor, and a short-circuit reflect, all located on the reference chip. The series resistor and series capacitor calibration structures used in this work were identical to those described in previous work by Orloff *et al.*,[24] and consisted of a 10 μm resistive strip embedded in the center conductor to define the series resistor, and a 10 μm gap in the center conductor to define the series capacitor. We first performed a multiline thru-reflect-line (TRL) calibration[25] to determine the propagation constant of the bare-CPW lines ($\gamma_0$), followed by the series-resistor calibration[24] to compute the capacitance per unit length of the bare CPW section ($C_0$) (Fig. 2E section-1). In the second-tier calibration, we measured all four microfluidic lines, as well as a single short-circuit reflect structure loaded by a microfluidic channel, all located on the test chip. We then performed a multiline TRL calibration[25] and de-embedding procedure[14,26] to obtain the propagation constant for the microfluidic channels ($\gamma_{tot}$) (Fig. 2E section-3).

The propagation constant for the bare CPW lines can be written as: $\gamma_0 = \sqrt{(R_0 + i\omega L_0)(G_0 + i\omega C_0)}$, where $\omega$ is the angular frequency and $R_0$, $L_0$, $G_0$, and $C_0$ are the distributed resistance, inductance, conductance, and capacitance per unit length of the bare-CPW lines respectively as a function of frequency. We can assume that $G_0 = 0$ because quartz has a negligible conductivity. Given a nonmagnetic fluid, $\gamma_{tot} = \sqrt{(R_0 + i\omega L_0)(G_{tot} + i\omega C_{tot})}$, where $R_0$ are $L_0$ came from the first-tier calibration of the bare CPW structures, and where $G_{tot}$ and $C_{tot}$ are the capacitance and conductance per unit length respectively of the microfluidic channels. We computed $G_{tot}$ and $C_{tot}$ using both $\gamma_{tot}$ and $\gamma_0$:[27]

 This journal is © The Royal Society of Chemistry 2017

Published on 04 July 2017. Downloaded by National Institutes of Standards & Technology on 2/26/2019 10:30:16 PM.

$$\left(\frac{\gamma_{tot}^{\ 2}}{\gamma_{0}^{\ 2}}\right)\cdot i\omega C_{0} = G_{tot} + i\omega C_{tot}. \quad (1)$$

The multiline-TRL calibration enables accurate measurements at microwave and mm-wave frequencies; the upper frequency limit of the measurements using our current approach is determined by the appearance of higher-order waveguide modes beyond the quasi-TEM mode. However, the multiline-TRL calibration method has a lower frequency limit determined by the length of the longest CPW line, and there are practical limits to how long we can make our CPW structures. Below 5 GHz, instead of using the multiline-TRL approach, we directly extracted the propagation constant of the channels through an alternative calibration process of de-embedding and distributed parameter fitting.[14,26]

De-embedding involves accounting for the impedance and propagation constant of cables, probes, and each section leading up to the microfluidic channels (Fig. 2B everything leading up to section-3). Information from the first-tier calibration accounts for these effects. Two different lengths of SU-8 covered sections on the test chips are used to account for the impedance and propagation constant of the SU-8 section (Fig. 2E section-2) between the bare CPW and fluid-filled channels. The procedures for determining uncertainties, both above and below 5 GHz, are detailed in the ESI.‡

### 2.4 Sample prep

We used serial dilution to prepare four concentrations of saline solutions: 30%, 3%, 0.3%, and 0.03% NaCl by weight ($W_{NaCl}$). We made the highest concentration by dissolving 428.6 g of NaCl in 1 L of deionized (DI) water, and then used DI water to make the other three dilutions. For context, normal/physiological saline is 0.9% NaCl,[28] typical sea water is ~3.5% NaCl, and the maximum solubility of NaCl in water at 20 °C is 35.9%.[29] Note that our maximum concentration ($W_{NaCl}$ = 30%) is near the solubility limit.

## 3 Results

We present calibrated fluid data as $C_{tot}$ and $G_{tot}/\omega$, since these quantities can be approximated as linearly proportional to the real and imaginary parts of the fluid permittivity ($\varepsilon_f'$ and $\varepsilon_f''$) respectively:

$$\varepsilon' = \left(C - C_{Air}\right)k + \varepsilon_0, \quad (2)$$

$$\varepsilon'' = \frac{G}{\omega}k. \quad (3)$$

Here $C_{Air}$ is the per unit length capacitance of an air-filled channel ($C_{Air}$ = 1.08 × $10^{-10}$ F $m^{-1}$), $\varepsilon_0$ is the permittivity of free space, and $k$ is a dimensionless geometric conversion factor that is specific to our devices. We used eqn (2) and literature values for the permittivity of de-ionized water[30] to compute a value for the geometric constant ($k$ = 0.411 ± 0.005). We also performed finite-element simulations[31] based on the measured dimensions of our devices to corroborate our estimation of $k$, and to validate eqn (2) and (3). While eqn (2) and (3) allow us to convert measured admittance parameters ($C$ and $G/\omega$) directly to permittivity values, we use permittivity only to describe intrinsic fluid properties and do not present measured data in terms of permittivity when EDL effects are present. The geometric constant $k$ will be used to determine the ionic conductivity of the measured solutions, as shown in the next section.

The resulting calibrated admittance per unit length data for air, DI water, and all concentrations of saline, as a function frequency, at a temperature of 28.6 ± 2 °C, are shown in Fig. 3. Additional measurements at 9.5 ± 2 °C and 47.6 ± 2 °C are shown in the ESI,‡ Fig. S1. We omitted data below a frequency where uncertainties rose above 2% of the measured value. We can qualitatively distinguish EDL effects from the intrinsic fluid admittance in the data as an increase and plateau of capacitance at lower frequencies (seen below ~1 GHz in $C_{tot}$ data for the $W_{NaCl}$ = 30% solution in Fig. 3) and as a suppression of conductance, also at lower frequencies (seen

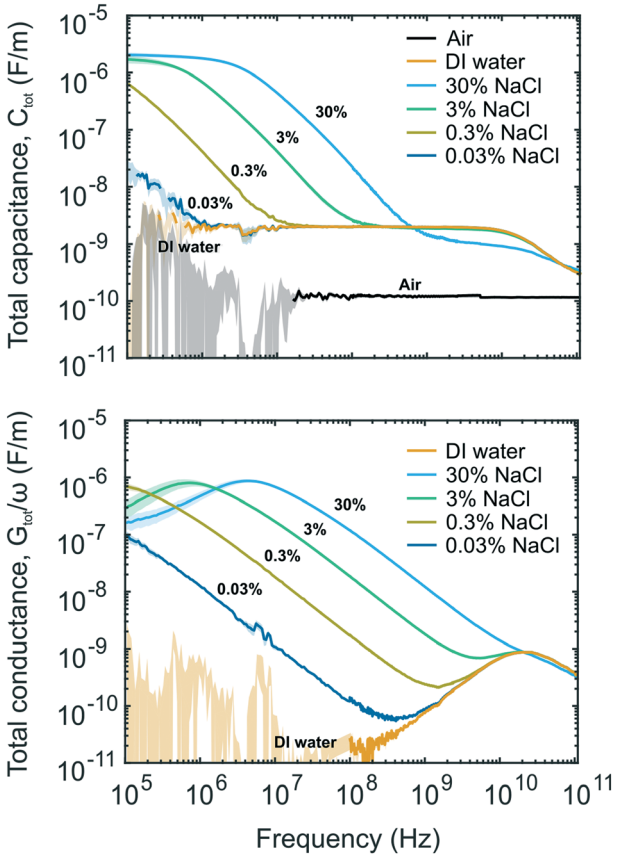


Fig. 3 Calibrated admittance per unit length data for DI water and four concentrations of NaCl solutions at 28.6 °C. Lighter shaded regions indicate uncertainties. Double-layer effects can be seen as an increase and plateau of capacitance at lower frequencies in $C_{tot}$ data, and a suppression of conductance in $G_{tot}/\omega$ data.

Published on 04 July 2017. Downloaded by National Institutes of Standards & Technology on 2/26/2019 10:30:16 PM.

below ~10 MHz in $G_{tot}$ data for the $W_{NaCl}$ = 30% solution in Fig. 3). We consider increases in $G_{tot}/\omega$ from the ionic conductivity of the fluid as part of the intrinsic response of the fluid. As we increased the ionic concentration in the solution, there was a corresponding increase in ionic conductivity as well as a shift in the EDL response to higher frequencies. The capacitance contribution from the EDL is significant compared to the fluid, up to ~3 orders of magnitude larger than the intrinsic capacitance of water.

### 3.1 Modeling the fluid admittance

For a given device, the total measured admittance can be written as $Y_{tot} = G_{tot} + i\omega C_{tot}$, (where the total measured impedance is $Z_{tot} = 1/Y_{tot}$). As shown in Fig. 4A, we assume that the EDL admittance ($Y_{EDL}$) acts in series with the fluid admittance ($Y_f$):

$$\frac{1}{Y_{eff}} = \frac{2}{Y_{EDL}} + \frac{1}{Y_f}. \quad (4)$$

We initially modeled the admittance of the fluid ($Y_f$) in the high-frequency regime, above an estimated minimum frequency where EDL effects can be neglected (Fig. 5A). We estimated the minimum frequency of this range using an iterative procedure, finding the lowest frequency that maximized the goodness of fit for a model that included only the fluid response. The fluid admittance of the saline solutions can be represented with the equivalent circuit shown in Fig. 4B, with three parallel components (all per unit length quantities): the capacitance of the fluid far above the relaxation frequency of the water ($C_\infty$), the dipolar contribution of the water ($C_w$), and the conductance due to the ions ($G_\sigma$). When measuring air, $C_\infty = C_{Air}$ and $G_\sigma = Y_w = 0$. The relaxation of water (seen at ~20 GHz in our data) is a Debye-type relaxation phenomenon, and thus can be modeled with a Cole–Cole function.[20–22,32] The total admittance of fluid ($Y_f$) was therefore:

$$Y_f = i\omega C_\infty + G_\sigma + Y_w = i\omega C_\infty + G_\sigma + i\omega \frac{C_w}{1 + (i\omega\tau_w)^{1-\alpha_w}}, \quad (5)$$

where $\tau_w$ is the rotational relaxation time of the water, and $\alpha_W$ is the broadening shape parameter of the water relaxation.

The resulting fit parameters for $Y_f$, obtained from the high frequency portion of the admittance spectra, for all ionic concentrations and all temperatures can be found in the ESI‡ (Table S1). All fits of $Y_f$ were within measurement uncertainties. For the highest ionic concentrations ($W_{NaCl}$ = 30% and 3%), we observed a noticeable suppression of the saline permittivity with increasing NaCl concentration (Fig. S2a‡). As we increased the temperature, we also observed both a suppression of the permittivity as well as a shift in the relaxation of the saline response to higher frequencies (Fig. S2b‡). We calculated fluid permittivity values using the conversion factor $k$ introduced previously. Our fit results for the permittivity of the lowest concentration of saline ($W_{NaCl}$ = 0.03%) (Table S1‡) are in close quantitative agreement with literature results for the permittivity of DI water.[30] Additionally, the same conversion factor k can be used to relate the conductance $G_\sigma$ to the bulk ionic conductivity of the solution: $G_\sigma = \sigma/k$, where $\sigma$ is the ionic conductivity of the fluid. The calculated conductivities of our solutions are given in Table S2 in the ESI.‡

### 3.2 Modeling the double-layer admittance

With a complete determination of $Y_f$, we solved eqn (4) for $Y_{EDL}$ (Fig. 5B) for each fluid sample. The extracted EDL admittance data were analyzed in the region below the frequency limit where $Y_{tot}$ deviated from the fit of $Y_f$ by more than 2% (Fig. 5B), *i.e.* where EDL effects begin to have a measureable effect. As shown in Fig. 4C, we modeled the EDL admittance ($Y_{EDL}$) as two parallel components (Fig. 4B): the primary component of the EDL response is a Debye-type relaxation, with admittance: $Y_D = C_D + i\omega G_D$, and a second

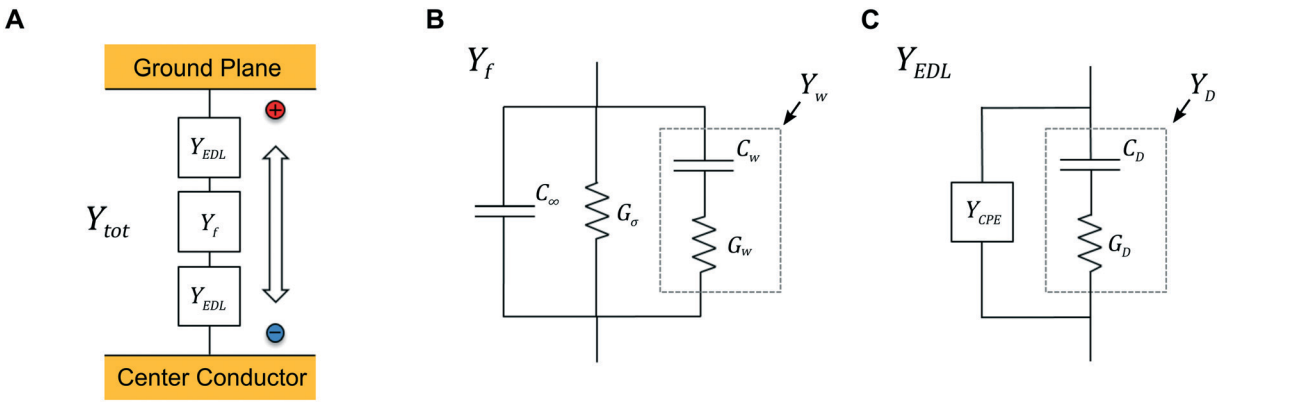


Fig. 4 Ionic fluid admittance model. (A) EDL admittance ($Y_{EDL}$) and fluid admittance ($Y_f$) act in series to form the measured admittance ($Y_{tot}$). (B) Equivalent circuit of $Y_f$, where $C_\infty$ is the capacitance of the fluid without the dipolar contribution of the water, $Y_w$ is the admittance from the dipolar response of the water, and $G_\sigma$ is the bulk conductance from the ions. (C) Equivalent circuit of $Y_{EDL}$, where $Y_D$ is the admittance of the Debye relaxation component of the EDL effect, and $Y_{CPE}$ is the admittance of the constant phase element (CPE).

 This journal is © The Royal Society of Chemistry 2017

Published on 04 July 2017. Downloaded by National Institutes of Standards & Technology on 2/26/2019 10:30:16 PM.

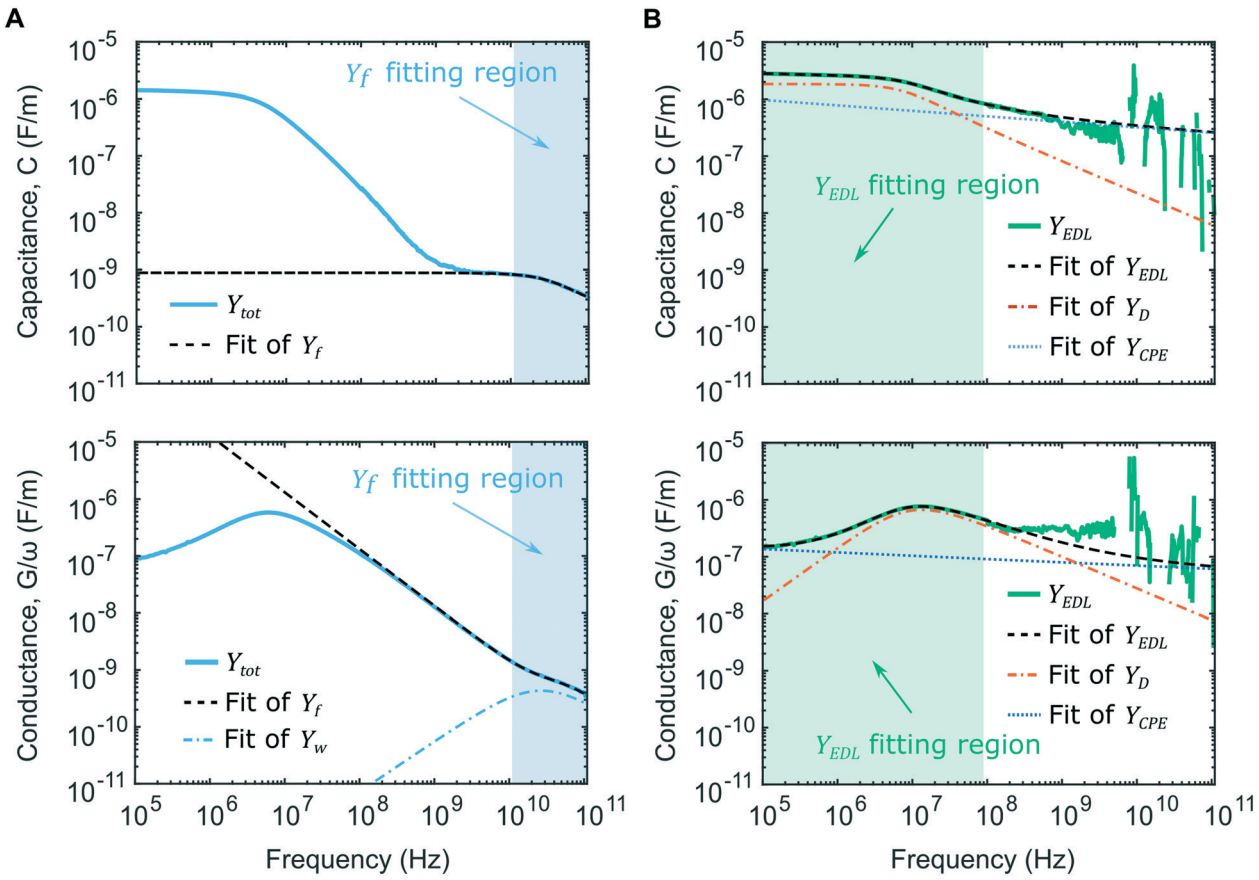


**Fig. 5** Fitting procedure using $W_{NaCl}$ = 30% data at 47.6 °C. (A) Data, and fit of the fluid admittance ($Y_f$), with contribution from water admittance ($Y_w$). (B) Extracted EDL admittance ($Y_{EDL}$), fit $Y_{EDL}$, Debye relaxation component of $Y_{EDL}$ ($Y_D$), and the CPE component of $Y_{EDL}$ ($Y_{CPE}$).

parallel contribution which we describe as a constant phase element ($Y_{CPE}$). The accumulation of ions at the surface of the electrodes result in a capacitance ($C_D$), with an associated conductivity term ($G_D$), which describes the immobility of the ions in proximity to the electrode surface. Like the Debye-type relaxation of water, $Y_D$ can be approximated by the Cole–Cole function, with an associated relaxation time constant $\tau_D$, and broadening shape parameter $\alpha_D$. The resulting expression for $Y_{EDL}$ is then:

$$Y_{EDL} = Y_{CPE} + \left(G_D + i\omega C_D\right) = Y_{CPE} + i\omega \frac{C_D}{1 + \left(i\omega\tau_D\right)^{1-\alpha_D}}, \quad (6)$$

Our analysis suggests that there is a second component to $Y_{EDL}$, which we show can be described with a constant phase element (CPE), with admittance ($Y_{CPE}$). This additional admittance term becomes important at lower frequencies, for higher conductivity solutions. The CPE contribution has most commonly been attributed to the electrode surface topography, *i.e.* surface roughness or porosity.[22] More recently, the CPE has been attributed to atomic scale inhomogeneities.[33] Regardless of physical interpretation, we observe a power-law frequency dependence in our data that can be modeled with a CPE term:

$$Y_{CPE} = Q\omega^{-n} e^{i\frac{\pi}{2}n}, \quad (7)$$

where $Q$ and $n$ are fitting parameters, and where $Q$ has the units [S m$^{-1}$ Hz$^n$].[34] The inclusion of $Y_{CPE}$ in the model (eqn (6)) was essential for getting an accurate fit of $Y_{EDL}$ over a broad range of frequencies and concentrations, and for an accurate determination of the time constant $\tau_D$. The resulting parameters from our fit of extracted $Y_{EDL}$ data, for all NaCl concentrations and all temperatures, using eqn (6) and (7), can be found in Table 1. The results for all fits to $Y_{EDL}$ were within measurement uncertainties.

We were only able to accurately model $Y_{CPE}$ effects for $W_{NaCl}$ = 30% and 3% solutions, which have a relaxation frequency ($\tau_D$) that was well above our minimum measurement frequency of 100 kHz. At lower concentrations, the contribution of CPE effects occurred at frequencies below the range used in these measurements. For these lower concentrations ($W_{NaCl}$ = 0.3% and 0.03%), we held $C_D$, $\alpha_D$, $Q$, and $n$ fixed using values from the fit of $W_{NaCl}$ = 3% data, while allowing $\tau_D$ to vary. This method produced fits for the $W_{NaCl}$ = 0.3% and 0.03% solutions that were comparable in goodness of fit to the $W_{NaCl}$ = 30% and 3% solutions. The phase of the CPE is given as: $\phi = n\frac{\pi}{2}$, where a purely capacitive effect has a phase of

Published on 04 July 2017. Downloaded by National Institutes of Standards & Technology on 2/26/2019 10:30:16 PM.

**Table 1** Parameters obtained from the fit of electrical double-layer (EDL) admittance *vs.* frequency (eqn (6)). The label "fixed" indicates that a parameter was held fixed while fitting the low concentration data using values from a previous fit of $W_{NaCl}$ = 3% data

| Temp (°C) | $W_{NaCl}$ (%) | $C_D$ (F m$^{-1}$) | $\tau_D$ (S) | $1 - \alpha_D$ | $Q$ (S m$^{-1}$ Hz$^n$) | $n$ |
|---|---|---|---|---|---|---|
| 9.5 | 30 | $1.91 \times 10^{-6}$ | $2.9 \times 10^{-8}$ | 0.89 | $3.7 \times 10^{-6}$ | −0.92 |
| | 3 | $2.25 \times 10^{-6}$ | $1.8 \times 10^{-7}$ | 0.79 | $8.7 \times 10^{-7}$ | −0.99 |
| | 0.3 | Fixed | $2.0 \times 10^{-6}$ | Fixed | Fixed | Fixed |
| | 0.03 | Fixed | $4.2 \times 10^{-5}$ | Fixed | Fixed | Fixed |
| 28.6 | 30 | $1.93 \times 10^{-6}$ | $1.6 \times 10^{-8}$ | 0.83 | $3.0 \times 10^{-6}$ | −0.92 |
| | 3 | $2.02 \times 10^{-6}$ | $1.1 \times 10^{-7}$ | 0.79 | $7.8 \times 10^{-7}$ | −0.99 |
| | 0.3 | Fixed | $1.1 \times 10^{-6}$ | Fixed | Fixed | Fixed |
| | 0.03 | Fixed | $2.5 \times 10^{-5}$ | Fixed | Fixed | Fixed |
| 47.6 | 30 | $1.87 \times 10^{-6}$ | $1.1 \times 10^{-8}$ | 0.87 | $2.3 \times 10^{-6}$ | −0.93 |
| | 3 | $1.93 \times 10^{-6}$ | $7.4 \times 10^{-7}$ | 0.81 | $1.2 \times 10^{-6}$ | −0.97 |
| | 0.3 | Fixed | $8.0 \times 10^{-6}$ | Fixed | Fixed | Fixed |
| | 0.03 | Fixed | $1.5 \times 10^{-5}$ | Fixed | Fixed | Fixed |

$\phi = \frac{\pi}{2}$ (90°). The phase angle of the CPE in our measurements was found to be ~83° for the $W_{NaCl}$ = 30% solution, and ~88° for the $W_{NaCl}$ = 3% solution and lower concentrations. A similar study of EDL effects in CPW devices performed by Hong *et al.* reported a CPE phase angle of ~76°.[35]

The fitting procedure described above yields an experimentally-determined frequency ($1/(2\pi\tau_D)$) that separates an EDL-dominated regime from a regime that reflects intrinsic fluid properties. This time scale, $\tau_D$, was interpreted as the characteristic charging time associated with the EDL, which was expected to be inversely proportional to solution conductivity.[18] To test the dependence on the solution conductivity, we show in Fig. 6 the results of a linear regression ($\tau_D = A\sigma^a$, where $A$ and $a$ were fitting parameters) for all NaCl concentrations and all temperatures. This linear regression produced the values of $A = 6.0 \pm 0.2 \times 10^{-7}$ (F m$^{-1}$) and $a = -1.0 \pm 0.05$, confirming our expectations that $\tau_D \propto \sigma^{-1}$.

These results demonstrate that the frequency-dependent EDL admittance in microfluidic devices can be accurately modeled with a time constant that can be predicted based on the ionic conductivity of the solution. To further illustrate this point, we show the $Y_D$ contribution to the EDL admittance for all temperatures and concentrations (Fig. 7), which we plotted as a function of frequency scaled by the experimentally-determined relaxation frequency ($\tau_D$). The collapse of the data for all concentrations and temperatures implies a single mechanism that gives rise to the $Y_D$ response, which can be accurately predicted by the solution conductivity. This in turn suggests that device-dependent EDL effects in microfluidic-based impedance measurements and sensors can be quantified by a single measurement of a fluid of known conductivity.

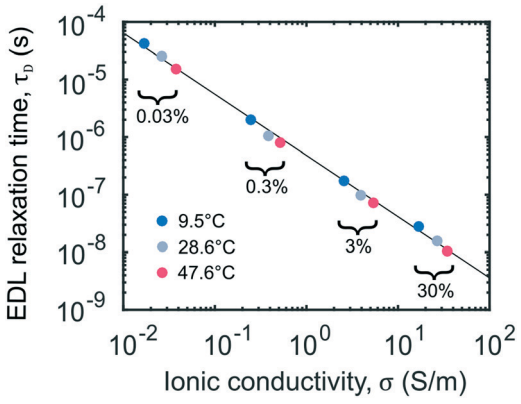


**Fig. 6** The electrical double-layer (EDL) relaxation time constants ($\tau_D$) *vs.* ionic conductivity ($\sigma$) for all NaCl concentrations and for all temperatures. A power law was used to fit the data ($\tau_{EDL} = A\sigma^a$), where $A$ = 6.0 ± 0.2 × 10$^{-7}$ and $a$ = −1.0 ± 0.05.

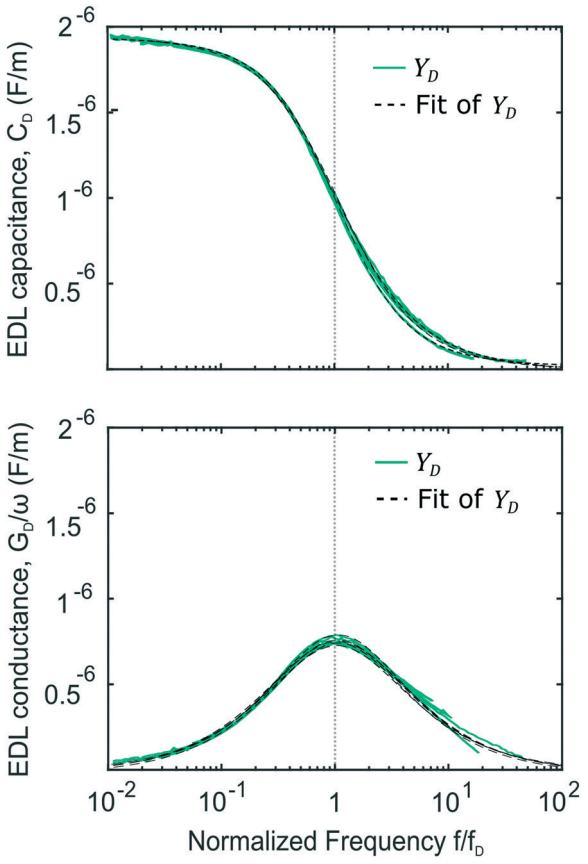


**Fig. 7** Extracted Debye relaxation component of the electrical double-layer (EDL) admittance with fit ($Y_D = Y_{EDL} - Y_{CPE}$) for $W_{NaCl}$ = 30%, 3%, and 0.3%, for temperatures of 9.5 °C, 28.6 °C, and 47.6 °C. Data is normalized to the EDL relaxation frequency ($1/(2\pi\tau_D)$).


This journal is © The Royal Society of Chemistry 2017

Published on 04 July 2017. Downloaded by National Institutes of Standards & Technology on 2/26/2019 10:30:16 PM.

# 4 Conclusions

Here, we used microfluidic-CPW devices and a calibration protocol to quantitatively determine the complex electrical impedance of saline-loaded transmission lines from 100 kHz to 110 GHz. The high frequency, broadband capabilities of our devices allowed the separation of the intrinsic fluid response from electrical double-layer effects. Our modeling of the electrical double-layer response confirms that the effect has two components: a Debye relaxation; and a constant phase element. We found that the derived relaxation time associated with the electrical double-layer was strictly inversely proportional to the ionic conductivity of the measured solutions. We also found that for concentrations at or below $W_{NaCl}$ = 3% the only parameter to change in any significant or measurable way was the electrical double-layer time constant. Knowing this allows us to fit for EDL parameters at one concentration and temperature, and extrapolate the electrical double-layer response to any other concentration and temperature, making it possible to distinguish EDL effects from other low-frequency phenomena. Future work on this topic will explore the effects of varying microwave power, mixtures of different ionic species, and varying geometry of the microfluidic coplanar waveguide devices.

# Acknowledgements

The authors wish to thank Dr. Angela C. Stelson, Dr. S. Russek, Dr. K. Keenan, K. Genter, I. Haygood, and Dr. C. Weil, all with the National Institute of Standards and Technology (NIST), for their critical feedback during the course of this research and for their comments on this manuscript. The authors thank Ms. Sarah E. Bonson, Mount St. Mary's University, MD, for fabricating the saline samples. The authors also thank Dr. A. Hagerstrom for his insightful discussions regarding this measurement technique and modeling of the electrical double layer effects.

# References

1 H. Fricke, *J. Gen. Physiol.*, 1925, **9**, 137–152.
2 S. Gawad, L. Schild and P. Renaud, *Lab Chip*, 2001, **1**, 76–82.
3 S. Afshar, E. Salimi, K. Braasch, M. Butler, D. J. Thomson and G. E. Bridges, *IEEE Trans. Microwave Theory Tech.*, 2016, **64**, 991–998.
4 S. C. Bürgel, C. Escobedo, N. Haandbæk and A. Hierlemann, *Sens. Actuators, B*, 2015, **210**, 82–90.
5 J. Chen, C. Xue, Y. Zhao, D. Chen, M.-H. Wu and J. Wang, *Int. J. Mol. Sci.*, 2015, **16**, 9804–9830.
6 D. Malleo, J. T. Nevill, L. P. Lee and H. Morgan, *Microfluid. Nanofluid.*, 2010, **9**, 191–198.
7 M. Evander, A. J. Ricco, J. Morser, G. T. A. Kovacs, L. L. K. Leung and L. Giovangrandi, *Lab Chip*, 2013, **13**, 722–729.
8 S. Abdalla, *J. Mol. Liq.*, 2011, **160**, 130–135.
9 K. Cheung, S. Gawad and P. Renaud, *Cytometry, Part A*, 2005, **65**, 124–132.
10 B. Eker, R. Meissner, A. Bertsch, K. Mehta and P. Renaud, *PLoS One*, 2013, **8**, e57423.
11 C. Küttel, E. Nascimento, N. Demierre, T. Silva, T. Braschler, P. Renaud and A. G. Oliva, *Acta Trop.*, 2007, **102**, 63–68.
12 E. Ermilova, F. F. Bier and R. Hölzel, *Phys. Chem. Chem. Phys.*, 2014, **16**, 11256–11264.
13 S. Tomić, S. D. Babić, T. Vuletić, S. Krča, D. Ivanković, L. Griparić and R. Podgornik, *Phys. Rev. E: Stat., Nonlinear, Soft Matter Phys.*, 2007, **75**, 021905.
14 J. C. Booth, N. D. Orloff, J. Mateu, M. Janezic, M. Rinehart and J. A. Beall, *IEEE Trans. Instrum. Meas.*, 2010, **59**, 3279–3288.
15 J. Mateu, N. Orloff, M. Rinehart and J. C. Booth, *2007 IEEE/MTT-S International Microwave Symposium*, 2007, pp. 523–526.
16 K. Grenier, D. Dubuc, P. E. Poleni, M. Kumemura, H. Toshiyoshi, T. Fujii and H. Fujita, *IEEE Trans. Microwave Theory Tech.*, 2009, **57**, 3246–3253.
17 I. Ocket, L. Song, D. Grillet, B. Embrechts, D. Schreurs, W. D. Raedt and B. Nauwelaers, *2013 IEEE Topical Conference on Biomedical Wireless Technologies, Networks, and Sensing Systems*, 2013, pp. 43–45.
18 M. Z. Bazant, K. Thornton and A. Ajdari, *Phys. Rev. E: Stat., Nonlinear, Soft Matter Phys.*, 2004, **70**, 021506.
19 T. Ragheb and L. A. Geddes, *Ann. Biomed. Eng.*, 1991, **19**, 151–163.
20 D. Jaron, H. P. Schwan and D. B. Geselowitz, *Med. Biol. Eng.*, 1968, **6**, 579–594.
21 R. P. Buck, *Ann. Biomed. Eng.*, 1992, **20**, 363–383.
22 T. Pajkossy, *J. Electroanal. Chem.*, 1994, **364**, 111–125.
23 Y. Xia and G. M. Whitesides, *Annu. Rev. Mater. Sci.*, 1998, **28**, 153–184.
24 N. D. Orloff, J. Mateu, A. Lewandowski, E. Rocas, J. King, D. Gu, X. Lu, C. Collado, I. Takeuchi and J. C. Booth, *IEEE Trans. Microwave Theory Tech.*, 2011, **59**, 188–195.
25 D. F. Williams, C. M. Wang and U. Arz, *IEEE MTT-S International Microwave Symposium Digest, 2003*, 2003, vol. 3, pp. 1819–1822.
26 S. Liu, I. Ocket, P. Barmuta, T. Markovic, A. Lewandowski, D. Schreurs and B. Nauwelaers, *84th ARFTG Microwave Measurement Conference*, 2014, pp. 1–5.
27 M. D. Janezic and D. F. Williams, *1997 IEEE MTT-S International Microwave Symposium Digest*, 1997, vol. 3, pp. 1343–1346.
28 *Mosby's Medical Dictionary*, 8th edn, 2009.
29 *CRC Handbook of Chemistry and Physics*, CRC Press/Taylor & Francis, Boca Raton, FL, 97th edn, 2017.
30 D. P. Fernández, Y. Mulev, A. R. H. Goodwin and J. M. H. L. Sengers, *J. Phys. Chem. Ref. Data*, 1995, **24**, 33–70.
31 N. Orloff, J. Mateu, M. Murakami, I. Takeuchi and J. C. Booth, *2007 IEEE/MTT-S International Microwave Symposium*, 2007, pp. 1177–1180.
32 R. Buchner, J. Barthel and J. Stauber, *Chem. Phys. Lett.*, 1999, **306**, 57–63.
33 Z. Kerner and T. Pajkossy, *J. Electroanal. Chem.*, 1998, **448**, 139–142.
34 J. Ross Macdonald, *Solid State Ionics*, 1984, **13**, 147–149.
35 J. Hong, D. Sung Yoon, S. Kwan Kim, T. Song Kim, S. Kim, E. Y. Pak and K. No, *Lab Chip*, 2005, **5**, 270–279.